Electronic Structure and Defect-Induced Properties of Oxygen-Deficient CaMnO3-δ: Insights from First-Principles Calculations

Citation for the original published paper (version of record):
Gastaldi, J., Brorsson, J., Hellman, A. et al (2026). Electronic Structure and Defect-Induced Properties of Oxygen-Deficient CaMnO3-δ: Insights from First-Principles Calculations. Journal of Physical Chemistry C, In Press.
http://dx.doi.org/10.1021/acs.jpcc.5c06816

THE JOURNAL OF PHYSICAL CHEMISTRY C
A JOURNAL OF THE AMERICAN CHEMICAL SOCIETY

pubs.acs.org/JPCC
Article

Electronic Structure and Defect-Induced Properties of Oxygen-Deficient $CaMnO_{3-\delta}$: Insights from First-Principles Calculations

Jonatan Gastaldi,* Joakim Brorsson, Anders Hellman, and Tobias Mattisson

Cite This: J. Phys. Chem. C 2026, 130, 1726−1735
Read Online

ACCESS | Metrics & More | Article Recommendations

ABSTRACT: Understanding the role of oxygen vacancies in perovskite oxides is essential for tailoring their functional properties. In this study, we employ density functional theory (DFT) calculations to investigate the structural, electronic, and defect-related properties of $CaMnO_{3-\delta}$ across a wide range of oxygen vacancy concentrations. Although prior studies have examined oxygen vacancies in $CaMnO_{3-\delta}$, here we present a systematic investigation across the full range from $\delta = 0$ to $\delta = 0.5$ in increments of $\Delta\delta = 0.0625$, thereby providing detailed new insights into its defect chemistry. Using cluster expansion techniques and high-accuracy relaxations, we identify ground-state configurations for each oxygen vacancy concentration and analyze their lattice distortions, bond length variations, and charge redistribution. Our results reveal a nonlinear progression of lattice parameters and bond environments with increasing oxygen vacancy concentration, accompanied by significant changes in the electronic band structure. Bader charge analysis indicates a progressive reduction in Mn oxidation state and charge compensation among all atomic species. As the estimated cost of creating oxygen vacancies increases at high concentration, from 2.03 to 2.26 eV, there exists a thermodynamic limit to vacancy incorporation at high oxygen vacancy concentrations. These findings provide a comprehensive understanding of how oxygen vacancies influence the stability and electronic behavior of $CaMnO_{3-\delta}$, offering insights relevant to its use in different types of applications.

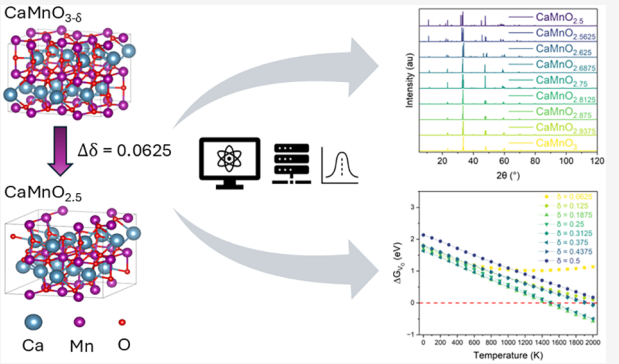

1. INTRODUCTION

Over the past decade, perovskites have been thoroughly studied because of their fundamental properties and potential practical applications, for example solar cells and other light sensitive processes[1−5] but also processes such as chemical-looping where perovskites can be used as oxygen-carriers.[6,7] Perovskite structures can be represented by the general formula $ABO_{3-\delta}$, where A is a larger alkaline or rare earth cation, B is a smaller transition metal cation, and δ represents the level of oxygen vacancies in the perovskite, which is related to the oxygen partial pressure in the surroundings. This type of material transfers oxygen without changing phase, unlike common monometallic oxygen carriers; a phenomenon that manifests itself as a nonstoichiometry (δ). Since multiple species can partially occupy both cationic sites, the number of potential combinations is enormous. In the past few years, different manganites have evoked the interest of scientists; among which calcium Manganite ($CaMnO_{3-\delta}$) has been extensively studied both experimentally and theoretically.[8−21] Specifically, this is due to its interesting electric and magnetic properties which are beneficial in a wide range of applications, for example solid oxide fuel cells, sensors, spintronic devices, and as an oxygen carrier in chemical-looping combustion (CLC) and related energy technologies.[15,22−29] The latter concepts are novel processes for combustion, gasification, hydrogen and chemical production where oxygen carriers are pivotal, and where perovskites like $CaMnO_3$ could play an important role.[30−32] Besides showing promising results in applications, this material is also cheap to synthesize in comparison to other synthesizable materials.[33] One major problem, however, is the long-term stability, as it tends to undergo an irreversible phase change to $CaMn_2O_4$ and Ca_2MnO_4 both under reducing and alternating reducing and oxidizing conditions.[34,35] These phases are not as beneficial as $CaMnO_{3-\delta}$ as they do not possess the beneficial perovskite structure and hence have different properties. These phases are less advantageous than $CaMnO_{3-\delta}$, as they lack the beneficial perovskite structure, which plays a crucial role in enabling the desirable structural and electronic properties in the material.

Received: October 2, 2025
Revised: December 4, 2025
Accepted: January 8, 2026
Published: January 19, 2026

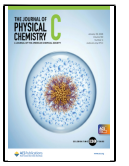

The presence of oxygen vacancies in $CaMnO_{3-\delta}$ can profoundly influence its material properties, leading to enhanced or altered functionalities. Oxygen vacancies are intrinsic defects that play a crucial role in determining the behavior of perovskite oxides: they can influence the electronic structure, magnetic ordering, ionic conductivity of the material and oxygen mobility. Understanding the effects of oxygen vacancies in $CaMnO_{3-\delta}$ is therefore essential for optimizing its performance in practical applications.

In this study we employ density functional theory (DFT) calculations using the Vienna Ab initio Simulation Package (VASP) to investigate the material properties of $CaMnO_{3-\delta}$ with and without oxygen vacancies. Previous work, such as that of Grimm and Bredow[16] has advanced the understanding of oxygen vacancies in $CaMnO_{3-\delta}$ by examining their effect on properties for different functionals. The present study extends this line of inquiry by providing a detailed account of vacancy behavior across a broad concentration range and including properties that have, to our knowledge, never been reported. We analyze the electronic structure and thermodynamic stability to provide a comprehensive understanding of how oxygen vacancies influence the behavior of $CaMnO_{3-\delta}$.

2. METHOD

2.1. Representative Structures

The most stable configuration of $CaMnO_3$ found in the Materials Project[36] database was used as a starting points for the first-principles calculations. Specifically, this corresponds to an orthorhombic structure, which belongs to space group 62 (*Pnma*). It is furthermore assumed to be ferromagnetic with a total magnetization of 3.0 μB per functional unit. The structural parameters and the unit cell of $CaMnO_3$ are presented in Figure 1.

a	5.33 Å
b	5.40 Å
c	7.57 Å
α	90.00°
β	90.00°
γ	90.00°
V	218.02 Å^3

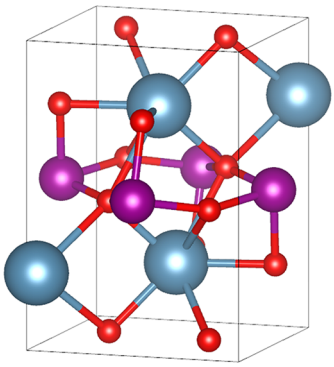

Figure 1. Structural parameters and the orthorhombic unit cell of $CaMnO_3$.

The orthorhombic unit cell of $CaMnO_3$ has a total of 20 atoms and the formula $Ca_4Mn_4O_{12}$. Since only stoichiometric $CaMnO_3$ is found in the database of Materials Project, the ground states for compositions with oxygen vacancies were determined using Cluster Expansions (CEs) as is described in Section 2.2.

2.2. Ground States

Here, the term "ground state" refers to the global lowest-energy configuration across all considered oxygen vacancy arrangements at a given composition, as obtained from the cluster expansion and mixed integer programming (MIP), and not to possible metastable electronic states within a single DFT + U calculation. The ICET toolkit[37] was used to find the ground state structures with oxygen vacancies via the creation of alloy CEs. This method is often used to represent disordered systems as combinations of clusters with different symmetries. Based on the order, or in other words, the number of atoms per cluster, these can be classified as pairs, triplets, quadruplets, and so on. Since the number of clusters is theoretically infinite, those above a certain order or with radii larger than specific cutoffs are disregarded. In practice, however, the selection is often limited by the available computational resources as well as the size of the training data set.

Here, 200 configurations were created by randomly replacing oxygen atoms in up to 40 atom $CaMnO_{3-\delta}$ supercells with vacancies. After relaxing the structures as detailed below, a CE, with cutoffs of 3.5 Å for pairs and 1.5 Å for triplets, was fitted using automatic relevance detection regression (ARDR). The ground states were then determined using a procedure based on MIP, as shown by Larsen et al.[38] and Brorsson et al.,[39] which is implemented in ICET.[37]

2.3. Computational Details

DFT, as implemented in VASP[40] (version 5.4.4), was used for all first-principles calculations, which includes structure relaxations and force determinations. The input files were, more precisely, generated with PYMATGEN.[41] This ensured that the settings were the same as in the Materials Project,[36] which entailed using the generalized gradient approximation (PBE + U) functionals presented by Perdew, Burke and Ernzerhof (PBE)[42] and an energy cutoff of 520 eV as well as setting the U-value for Mn to 3.9 eV.[41] A fixed U parameter is used for all compositions. Although a δ-dependent U may refine the accuracy, a constant U ensures consistency across stoichiometries and is appropriate for the comparative trends examined here. Initially, the energy differences for the electronic and ionic convergence were set to 10^{-3} eV and 10^{-2} eV per atom, respectively. After this, a second relaxation was performed using the same functionals, to achieve more accurate results, where the same thresholds were set to 10^{-6} eV and 10^{-5} eV.

Reciprocal grids of 1100 *k*-points per atom, which is higher than the default setting in the Materials Project (1000), were generated using the Monkhorst−Pack principle in the case of stoichiometric $CaMnO_3$ and the γ-centered method for each oxygen vacancy concentration. The tetrahedron method with Blöchl corrections, but without smearing, was used to sample the grid for all compositions.

This study concerns the following compositions, with different fractions of vacancies: $CaMnO_3$, $CaMnO_{2.9375}$, $CaMnO_{2.875}$, $CaMnO_{2.8125}$, $CaMnO_{2.75}$, $CaMnO_{2.6875}$, $CaMnO_{2.625}$, $CaMnO_{2.5625}$, $CaMnO_{2.5}$. In practice, 2 × 2 × 1 Super cells with up to 80 atoms were used in all calculations, specifically $Ca_{16}Mn_{16}O_{48}$, $Ca_{16}Mn_{16}O_{47}$, $Ca_{16}Mn_{16}O_{46}$, $Ca_{16}Mn_{16}O_{45}$, $Ca_{16}Mn_{16}O_{44}$, $Ca_{16}Mn_{16}O_{43}$, $Ca_{16}Mn_{16}O_{42}$, $Ca_{16}Mn_{16}O_{41}$, and $Ca_{16}Mn_{16}O_{40}$.

2.4. Oxygen Vacancy Formation Energy

The formation energy of oxygen vacancies (E_{V_O}) is defined as

$$E_{V_O} = \frac{1}{n}\left(E_{CaMnO_{3-\delta}} - E_{CaMnO_3} + \frac{n}{2}E_{O_2}\right) \quad (1)$$

https://doi.org/10.1021/acs.jpcc.5c06816
J. Phys. Chem. C 2026, 130, 1726−1735

for $CaMnO_3$. Here, E_{CaMnO_3} is the total energy of the stoichiometric $CaMnO_3$, $E_{CaMnO_{3-\delta}}$ is the total energy of $CaMnO_{3-\delta}$ with one or more oxygen vacancies and n represents the number of O atoms released by the structure. E_{O2} is the total energy of an O_2 molecule in the gas phase. The energy of the O_2 molecule, in vacuum, was optimized based on a cubic unit cell with a length of 20 Å. The methodology previously described for $CaMnO_{3-\delta}$ was also used for O_2, except that the volume of the cell was kept constant.

2.5. Temperature-Dependent Gibbs Free Energy of Vacancy Formation

It is interesting to study the Gibbs Free Energy of an oxygen vacancy, ΔG_{V_O}, as a function of temperature and oxygen partial pressure

$$\Delta G_{V_O}(T, p_{O_2}) = \frac{1}{n}\left(E_{CaMnO_{3-\delta}} - E_{CaMnO_3} + F^{vib}_{CaMnO_{3-\delta}}(T) - F^{vib}_{CaMnO_3}(T) + \frac{n}{2}\mu_{O_2}(T, p)\right) \quad (2)$$

Where F^{vib} represents the vibrational free energy, which was obtained from phonon calculations based on the harmonic approximation, using Phonopy,[43] and included both phonon entropy and zero-point energy. The chemical potential of oxygen was estimated using the equation[44]

$$\mu_{O_2}(T, p) = E_{O_2} + \mu^{corr}_{O_2}(T) + k_B T \ln\left(\frac{p}{p^0}\right) \quad (3)$$

The thermal contribution, $\mu^{corr}_{O_2}$, was taken from the NIST-JANAF thermochemical tables to account for the temperature variation of the enthalpy and entropy.[45] The pressure correction, $k_B T ln\left(\frac{p}{p^0}\right)$, accounts for the difference between the actual pressure (p) and the standard reference pressure (p^0).

All calculations were performed under the assumption of neutral oxygen vacancies in the bulk perovskite structure for the purpose of isolating their impact without introducing additional complexity from charge compensation.

2.6. Electronic Band Structure

After relaxing the structures using PBE + U, as laid out in Section 2.3, a nonself-consistent calculation was performed using the Modified Becke-Johnson (MBJ) MetaGGA potential.[46] It should be emphasized that the MBJ potential is used exclusively for computing the electronic band structure, while all total energies and thermodynamic quantities throughout this work are obtained from PBE + U calculations, as it is known to produce more accurate band gaps than PBE + U for many transition-metal oxides, which includes $CaMnO_3$. In particular, PBE + U typically underestimates the band gap, whereas MBJ provides a band structure in closer agreement with available experimental data as shown by Becke and Johnson, and Tran, Blaha and Schwarz.[46,47] For this reason, structural relaxations and all total-energy quantities are obtained using PBE + U, while MBJ is employed only for the final nonself-consistent band-structure calculation. The MBJ calculations were performed with the same level of accuracy as the relaxations described in section 2.3 and using the default values for the MBJ parameters: $\alpha = -0.012$, $\beta = 1.023$ bohr$^{1/2}$, and e = 0.5. The band structure was calculated along the high-symmetry Brillouin zone path Γ—X—S—Y—Γ—Z—U—R—T—Z, which is continuous for members of space group 62 (*Pnma*), such as orthorhombic $CaMnO_3$, and visualized using the Python toolkit Sumo.[48] The same k-point grid was used for all oxygen vacancy concentrations to ensure a consistent k-point density, since the supercell dimensions were kept fixed. The choice of k-point mesh depends on the supercell dimensions and is therefore appropriate even when local symmetry lowering occurs in vacancy-ordered configurations.

3. RESULTS AND DISCUSSION

3.1. Structural Properties

The calculated lattice parameters from this work of stoichiometric $CaMnO_3$ are compared with two experimental data sets[8,9] and two previous computational studies[13,17] in Table 1. The a, b, and c parameters from this work (5.325 Å, 5.398 Å, and 7.554 Å, respectively) are slightly larger than the experimental and those predicted by previous calculations. The comparison reveals that the values obtained here fall within the expected range and show reasonable agreement with both experimental and theoretical references especially considering the theoretical references assumed antiferromagnetic magnetism compared to the ferromagnetism in this study. Differences in calculated lattice parameters depending on choice of magnetism has been shown to deviate 1−2%, which is the same magnitude as the difference between this study and previous theoretical studies. No previous studies on orthorhombic $CaMnO_3$ using ferromagnetic ordering was found in the literature.

Table 1. Comparison of Lattice Parameters and Volume of Stoichiometric $CaMnO_3$

δ	Exp.[8]	Exp.[9]	Calc.[13]	Calc.[17]	this work
a (Å)	5.264	5.286	5.316	5.314	5.325
b (Å)	5.279	5.292	5.380	5.367	5.398
c (Å)	7.448	7.463	7.543	7.548	7.554
V (Å^3)	206.97	208.77	215.73	215.26	217.11

The unit cell volume calculated in this work (217.11 Å^3) is larger than all other reported values, consistent with the expanded lattice parameters. Several factors may contribute to these differences. For example, the choice of exchange-correlation functional plays a significant role; the present work employs PBE + U, which is known to slightly overestimate lattice parameters compared to experiment. The small deviations from experimental values are within acceptable limits for DFT-based methods and support the validity of the subsequent analyses. Another factor is the assumed magnetic ordering. Here it was assumed to be ferromagnetic, but in experimental studies it may not have been explicitly reported or controlled. Additionally, minor deviations in oxygen stoichiometry (δ in $CaMnO_{3-\delta}$) in experimental samples can affect lattice dimensions, while calculations assume perfect stoichiometry. Finally, differences in computational setups such as k-point grids, energy cutoff, and pseudopotentials may also contribute to the observed variations across studies.

The calculated lattice parameters of $CaMnO_{3-\delta}$ reveal a structural response as the oxygen vacancy concentration increases, as shown in Table 2. As δ increases from 0 to 0.5,

https://doi.org/10.1021/acs.jpcc.5c06816
J. Phys. Chem. C 2026, 130, 1726−1735

Table 2. Lattice Parameters of Relaxed $CaMnO_{3-\delta}$ Structures

δ	0	0.0625	0.125	0.1875	0.25	0.3125	0.375	0.4375	0.5
a (Å)	5.325	5.348	5.375	5.383	5.454	5.431	5.422	5.375	5.392
b (Å)	5.398	5.416	5.429	5.419	5.328	5.400	5.415	5.346	5.382
c (Å)	7.554	7.554	7.561	7.554	7.625	7.650	7.467	7.948	8.026
α (°)	90.0	90.086	90.162	90.0	90.713	90.441	90.0	89.92	90.152
β (°)	90.0	89.949	90.056	90.0	90.0	90.253	90.0	90.12	92.321
γ (°)	90.0	89.657	89.755	90.364	90.004	89.855	92.105	89.569	89.996
V (Å^3)	217.11	218.74	220.64	220.33	221.57	224.35	219.08	228.35	232.67

Table 3. Average, Minimum, and Maximum Bond Lengths between Mn−O and Ca−O in $CaMnO_{3-\delta}$

δ	0	0.0625	0.125	0.1875	0.25	0.3125	0.375	0.4375	0.5
Mn−O (Å) (avg)	1.94	1.95	1.95	1.95	1.96	1.97	1.96	1.98	2.02
Mn−O (Å) (min)	1.94	1.90	1.83	1.89	1.90	1.89	1.89	1.88	1.87
Mn−O (Å) (max)	1.95	1.98	2.01	2.01	2.07	2.17	2.15	2.22	2.38
Ca−O (Å) (avg)	2.46	2.48	2.48	2.53	2.54	2.52	2.56	2.57	2.51
Ca−O (Å) (min)	2.32	2.27	2.26	2.26	2.29	2.29	2.29	2.32	2.26
Ca−O (Å) (max)	2.63	2.99	2.99	2.99	2.99	2.99	2.97	2.94	2.88

the lattice undergoes anisotropic distortions, reflecting the system's effort to accommodate the removal of oxygen atoms.

The a and b lattice constants exhibit moderate fluctuations. The a lattice constant increases steadily up to δ = 0.25, suggesting a gradual expansion along this axis, followed by a slight contraction at higher vacancy levels. The b parameter shows a less consistent trend, with minor increases and decreases, indicating localized structural adjustments rather than a uniform response.

In contrast, the c parameter remains relatively stable at low δ but decreases significantly at δ = 0.375 only to increase again, reaching its maximum at δ = 0.5. The elongation along the c-axis may signal that a more substantial structural rearrangement occurs at higher vacancy concentrations.

The lattice angles α, β, and γ, which are 90° in the ideal orthorhombic structure, begin to deviate slightly as δ increases. These deviations become more pronounced at higher vacancy levels, particularly in γ, which reaches 92.1° at δ = 0.375, and β, which is 92.3° at δ = 0.5. Such angular distortions suggest a change away from ideal symmetry, likely due to octahedral tilting induced by the vacancies.

Overall, the observed trends indicate that the introduction of oxygen vacancies leads to a complex, nonlinear structural evolution. These changes reflect the interplay between lattice relaxation, defect accommodation, and symmetry breaking within the structure.

In the stoichiometric $CaMnO_3$ structure, the Mn−O bond lengths are relatively uniform and fall within a narrow range. However, upon introducing oxygen vacancies, the difference between the maximum and minimum Mn−O bond lengths increases significantly. This indicates local distortions in the MnO_6 octahedra. Similarly, the Ca−O bond lengths show increased variation, suggesting changes in the coordination environment of calcium atoms. The estimated bond lengths of Mn−O and Ca−O in the supercells are presented in Table 3. Additionally, the distances between Mn atoms also change, which can influence the magnetic interactions and overall stability of the material.

3.2. Electronic Properties

The electronic band structure and total density of states (DOS) for stoichiometric $CaMnO_3$ and eight oxygen-deficient structures ($CaMnO_{3-\delta}$, δ = 0.0625 to 0.5) were calculated to evaluate the effects of oxygen vacancies on the material's electronic properties. The results, presented in Figures 2 and 3, reveal significant effects on the bandgap and electronic states induced by increasing oxygen deficiency.

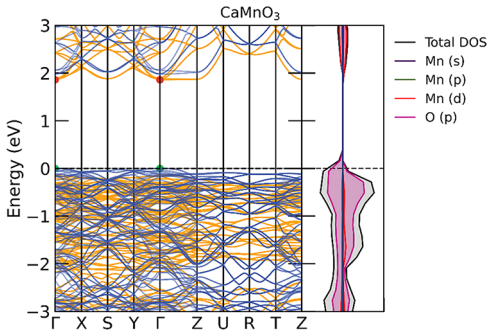

Figure 2. Band structure and DOS-plot for stoichiometric $CaMnO_3$. Orange bands represent spin-up and blue spin-down, while the red dot is the lowest point of the conduction bands and the green dot the highest point of the valence band. The reason that the DOS does not align perfectly with the valence band maximum (VBM) is because SUMO does not shift it according to sigma smearing since version 2.3.0.

For stoichiometric $CaMnO_3$, the band structure exhibits a direct bandgap of approximately 1.8 eV at the Γ-point. This would make it a semiconductor and is within the range of band gaps, i.e., from 1.02 eV to as high as 3.63 eV, where stoichiometric $CaMnO_3$ was estimated experimentally.[17,20,49] Previous DFT studies of stoichiometric $CaMnO_3$ found a band gap between 0.5 to 3.0 eV,[11,13,50,51] based on calculations with similar levels of accuracy as in this study.

The band gap for each oxygen vacancy concentration is presented in Table 4. Upon introducing oxygen vacancies (δ > 0) the bandgap decreases. At δ = 0.0625 the band gap becomes indirect and is reduced to around 0.9 eV. For δ = 0.125, it is still indirect and even smaller, close to 0.4 eV. At δ = 0.1875 the band gap has closed completely, meaning that $CaMnO_{2.8125}$ has a state similar to a metal. Interestingly enough, the band gap reopens as the level of oxygen vacancies increases further and stays so, but displays strong variations, until δ = 0.4375, where it closes, before opening again at δ = 0.5.

https://doi.org/10.1021/acs.jpcc.5c06816
J. Phys. Chem. C 2026, 130, 1726−1735

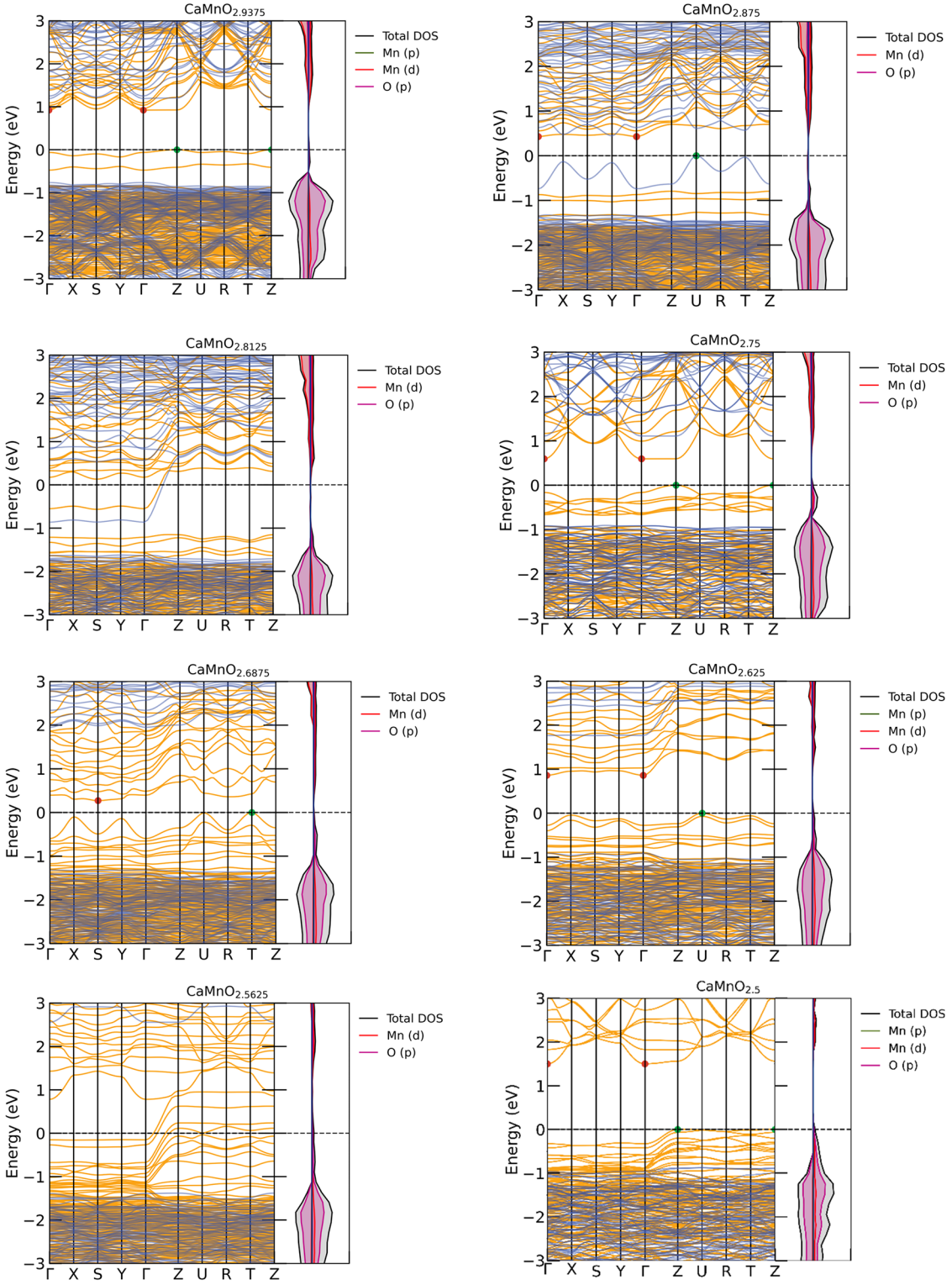

Figure 3. Band structure and DOS for $CaMnO_{3-\delta}$. The orange lines represent spin-up and blue spin-down, while the red dot is the lowest point of the conduction bands and the green dot the highest point of the valence bands.

Table 4. Band Gap in $CaMnO_{3-\delta}$

δ	0	0.0625	0.125	0.1875	0.25	0.3125	0.375	0.4375	0.5
E_g (eV)	1.86	0.92	0.42		0.59	0.21	0.86		1.5

The total DOS, shown alongside the band structures in Figures 2 and 3, complements these observations by highlighting the redistribution of electronic states. As δ increases, the total DOS near the Fermi level increases. This trend is particularly pronounced for $\delta = 0.375$ and $\delta = 0.5$, for which the Fermi level intersects the defect-induced states,

https://doi.org/10.1021/acs.jpcc.5c06816
J. Phys. Chem. C 2026, 130, 1726−1735

Table 5. Average Bader Net Charges for Each Atom-Type and Oxygen Vacancy Concentration

δ	0	0.0625	0.125	0.1875	0.25	0.3125	0.375	0.4375	0.5
Ca (e)	1.674	1.674	1.673	1.672	1.668	1.667	1.667	1.666	1.660
Mn (e)	2.240	2.204	2.170	2.133	2.113	2.068	2.033	2.007	1.976
O (e)	−1.305	−1.320	−1.337	−1.353	−1.375	−1.390	−1.410	−1.434	−1.455

Table 6. Oxygen Vacancy Formation Energies per Oxygen Vacancy at 0 K

δ	0	0.0625	0.125	0.1875	0.25	0.3125	0.375	0.4375	0.5
E_{V_O}(eV)		2.03	2.01	1.83	1.89	1.95	1.75	1.95	2.26

marking a transition to a semimetallic or metallic state. These changes are attributed to the increased electron density introduced by oxygen vacancies and the resulting local lattice distortions.

The progressive reduction in the bandgap and the appearance of defect states with increasing δ highlight the critical role of oxygen vacancies in tailoring the electronic properties of $CaMnO_{3-\delta}$ and the importance of studying oxygen vacancies on a fine grid, since key material properties can emerge only at specific concentrations. The narrowing of the bandgap and eventual metallization suggest potential applications in electronic devices where tunable conductivity is required.

3.3. Bader Charge Analysis

The average Bader net charges are listed in Table 5 for the different levels of δ. The Bader charge analysis reveals systematic changes in the electronic environment of $CaMnO_3$ as oxygen vacancies are introduced. These trends provide insight into how the system redistributes charge to maintain electrostatic balance in response to oxygen deficiency.

At δ = 0 (stoichiometric $CaMnO_3$), the average Bader charges are approximately +1.674 e for Ca, + 2.240 e for Mn, and −1.305 e for O. As δ increases, the average net charge on Mn atoms decreases steadily, reaching +1.976 e at δ = 0.5. This reduction reflects a lowering of the Mn oxidation state, consistent with the idea that electrons previously involved in ionic bounds involving the missing oxygen atoms have a tendency to localize on Mn, partially reducing Mn^{4+} to Mn^{3+}.

The Ca atoms also show a slight but consistent decrease in net charge, from +1.674e to +1.660e. Although less prominent than for Mn, this suggests that Ca may participate marginally in the charge redistribution.

In contrast, the average Bader charge on the remaining oxygen atoms becomes increasingly negative, shifting from −1.305e to −1.455e. This indicates that the remaining O atoms accommodate more electron density as vacancies are introduced, as evidenced by the increasingly negative Bader charges of the oxygen atoms.

Overall, these trends indicate that the charge compensation involves all three atomic species and that the redistribution of electron density helps stabilize the structure in the presence of oxygen vacancies.

3.4. Oxygen Vacancy Formation Energies

The formation energy of oxygen vacancies in $CaMnO_3$ was calculated for vacancy concentrations (δ) between 0 and 0.5. The results presented in Table 6 reveal a nonlinear increase in the vacancy formation energy with δ, indicating a progressively higher energy cost associated with introducing additional vacancies. This trend can be broken into three distinct ranges, more precisely low (δ = 0.0625 to 0.1875), medium (δ = 0.25 to 0.375), and high (δ = 0.25 to 0.375) levels of oxygen vacancies.

At low oxygen vacancy concentrations, the formation energy remains fairly consistent from 2.03 to 2.01 eV. This suggests that the crystal structure can initially accommodate oxygen vacancies with moderate energy penalties, likely due to local relaxation mechanisms or the inherent defect tolerance of the perovskite lattice. It should be noted that a formation energy of 2.03 eV is fairly high, which means that vacancies should not be expected to form spontaneously, which is consistent with results from previous calculations.[12] Since the data in Table 6 applies to the most stable structures at 0 K, the formation energy for oxygen vacancies may decrease at elevated temperatures due to entropic contributions and thermal effects.

As the vacancy concentration approaches a medium level, the formation energy per O atom is lower compared to δ = 0.0625 and 0.125, showing oxygen of 1.83−1.95 eV, with the exception of δ = 0.375, which has the lowest formation energy per O atom at 1.75 eV.

At high concentrations, the formation energy increases sharply, reaching 2.26 eV per O atom at δ = 0.5, which indicates a significant energy barrier. This suggests that the material could be approaching a limit, in terms of structural stability, or begins to favor the formation of alternative phases or defect arrangements.

These results highlight the importance of considering vacancy concentration when evaluating the thermodynamic stability of oxygen-deficient $CaMnO_3$. The increasing formation energy with δ suggests that while low levels of vacancies may be thermodynamically accessible, higher concentrations are likely to require nonequilibrium synthesis conditions or may lead to phase transformations. Compared to the low concentration zone, the increase in formation energy is significantly smaller from δ = 0.3125 to 0.375, but almost doubles from δ = 0.375 to 0.4375. This could indicate a higher level of stability for δ = 0.375 and that $CaMnO_3$ starts to shift into another phase beyond this point, which has, in fact, been observed in experiments.[34]

3.5. Gibbs Free Energies of Vacancy Formation

Calcium Manganite has been suggested as an oxygen carrier for chemical-looping combustion and could be relevant for other similar technologies at higher temperatures. Here, it is mainly the oxygen transfer capability which is of interest. Figure 4 illustrates the calculated Gibbs free energy of oxygen vacancy formation (ΔG_{V_O}) in $CaMnO_{3-\delta}$ over a temperature range of 0−2000 K for an oxygen partial pressure of 10^{-2} bar. These conditions are relevant in chemical-looping combustion (CLC) environments, where oxygen carriers operate under both oxidizing and reducing atmospheres.[34]

https://doi.org/10.1021/acs.jpcc.5c06816
J. Phys. Chem. C 2026, 130, 1726−1735

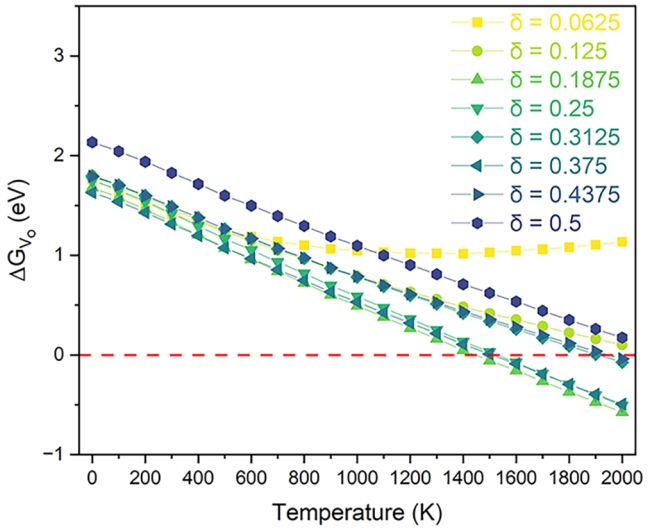

Figure 4. Gibbs free energy of oxygen vacancy formation per number of O atoms removed for $CaMnO_{3-\delta}$ with different oxygen vacancy concentrations for a partial oxygen pressure of 10^{-2} bar.

At low temperatures, ΔG_{V_O} remains positive across all pressures, indicating that oxygen vacancy formation is thermodynamically unfavorable in the bulk perovskite structure for all oxygen vacancy levels. As temperature increases, ΔG_{V_O} decreases due to the entropic contribution from the oxygen chemical potential. The transition to negative ΔG_{V_O}, where vacancy formation becomes favorable, occurs at 1400−1500 K for δ = 0.1875, 0.25 and 0.375, 1900 K for δ = 0.3125 and 0.4375. In the case of δ = 0.0625, 0.125, and 0.5, ΔG_{V_O} never goes below 0 eV, indicating that it is not thermodynamically favorable to remove the equivalent of 1, 2, or 8 oxygen atoms from a $Ca_{16}Mn_{16}O_{48}$ supercell. The behavior of δ = 0.0625 is peculiar as it does not follow a linear evolution of the Gibbs free energy as the temperature increases. This behavior is explained because the F^{vib} of δ = 0.0625 becomes higher than at δ = 0 around 500 K, and this shifts the change in Gibbs free energy and leads to what is seen in Figure 4.

The calculated Gibbs free energy of oxygen vacancy formation in $CaMnO_3$ reveals important insights into the thermodynamic behavior of this material under conditions relevant to chemical-looping processes. Our results show that ΔG_{V_O} remains positive across a wide temperature range and only becomes negative, and therefore thermodynamically favorable, at elevated temperatures and low oxygen partial pressures. This trend is consistent with the fairly strong bonding of oxygen in the bulk perovskite structure and highlights the inherent stability of stoichiometric $CaMnO_3$.

However, these findings differ from experimental observations, where oxygen release from $CaMnO_3$-based materials is reported at significantly lower temperatures (700−1000 K) under reducing conditions.[22,23] This discrepancy suggests that oxygen vacancy formation in real systems is not only affected by bulk thermodynamics. A few potential factors that could influence this are effects from surfaces or interfaces and structural transitions. Oxygen vacancies may form more readily at surfaces, grain boundaries, or other extended defects, where the local bonding environment is less constrained than in the bulk. These regions are not captured in our current bulk model but can be highly relevant in practical applications. Moreover, $CaMnO_3$ is known to undergo temperature-induced structural distortions, which could facilitate oxygen mobility or stabilize nonstoichiometric phases. Such transitions could lower the effective energy barrier for oxygen release. It has also been suggested that impurities or dopants, such as Fe and Ti, could influence the properties of $CaMnO_3$, and most experimental investigations have actively incorporated dopants or utilized technical grade or natural materials during production, where active impurities may be present.[52,53]

Taken together, these considerations suggest that while bulk $CaMnO_3$ exhibits strong resistance to vacancy formation, compared to experiments, real-world oxygen release likely involves a combination of surface processes, structural rearrangements, and potentially other effects that influence the stability of the material. Future work that incorporates surface models, additional phases, and machine learning potentials, to explore a wider range of potential interactions, could provide a more comprehensive understanding of oxygen transport and release in $CaMnO_3$.

3.6. Powder X-ray Diffraction Patterns

To support the structural models obtained from DFT calculations, we simulated Powder X-ray diffraction (PXRD) patterns based on the relaxed $CaMnO_{3-\delta}$ structures using the VESTA software.[54] These simulated patterns serve as theoretical fingerprints, allowing for qualitative comparison with experimental observations reported in the literature. PXRD is a widely used experimental technique for phase identification and has been previously used to characterize $CaMnO_3$. By simulating PXRD patterns for each oxygen vacancy level, we can ascertain if the induced structural changes are detectable. We note that the vacancy configurations used here originate from cluster expansion predictions of the lowest energy ordered arrangements and therefore impose a periodic ordering of vacancies. Such ordering necessarily lowers the symmetry locally, even when experiments indicate that vacancies are likely disordered and the average structure remains as *Pnma* for $\delta \leq 0.5$ The simulations were performed using a wavelength of 1.5406 Å, which corresponds to Cu Kα radiation. The results are shown in Figure 5. The simulated PXRD pattern for stoichiometric $CaMnO_3$ shows strong agreement with experimental data reported in the literature, particularly in the positions and relative intensities of the main diffraction peaks. This

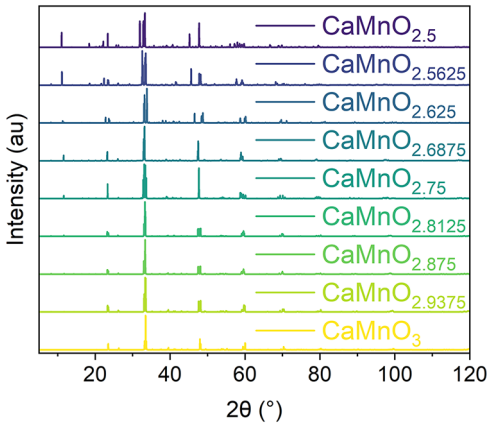

Figure 5. Simulated PXRD patterns for $CaMnO_{3-\delta}$.

https://doi.org/10.1021/acs.jpcc.5c06816
J. Phys. Chem. C 2026, 130, 1726−1735

agreement validates the structural model used in our simulations and provides a reliable baseline for analyzing the effects of oxygen vacancies. Notably, the prominent peaks around 2θ = 34°, 48°, and 59° in the simulated PXRD are close to the expected experimental peaks at 2θ = 34°, 48°, and 60°, confirming the orthorhombic perovskite structure (*Pnma* space group) of $CaMnO_3$.

At low oxygen vacancy concentrations, the PXRD patterns remain largely consistent with stoichiometric $CaMnO_3$, suggesting minimal structural distortion. At δ = 0.375, however, there is a noticeable change, since the peaks at around 34° and 48° have split. There are indications that this also applies to the 60° peak but because of low intensity, it is difficult to determine the significance. The splits remain at higher levels of oxygen vacancies and represent large enough shifts in the crystal structure to be observable in the PXRD patterns.

This effect has been reported by Poeppelmeier et al.[8] for δ = 0.5, but our results suggests that this structure change should be expected even at lower concentrations of oxygen vacancies. Further studies at a higher resolution might give more details about exactly when this shift occurs but would require significantly higher computational cost since the unit cells would need to include at least 140−160 atoms. Caution is, in other words, warranted when performing PXRD analyses of $CaMnO_3$, and possibly other perovskites, as the material can be mischaracterized if the shifted peaks are similar to another known phase. It is, for instance, known that $CaMnO_3$ can decompose into other phases, such as Ca_2MnO_4 and $CaMn_2O_4$[34] or $Ca_3Mn_2O_7$,[55] at high temperatures. Furthermore, the PXRD patterns for nonstoichiometric $CaMnO_3$ show similarities to those of Ca_2MnO_4, $Ca_2MnO_{3.5}$, and $Ca_3Mn_2O_7$,[8,56−60] with high double peaks between 30 and 35° and 45−50°, suggesting a possible structural convergence or phase transition. This should be interpreted as a local symmetry lowering effect in the ground-state configurations, rather than a prediction that long-range symmetry breaking must occur experimentally at low δ.

4. CONCLUSIONS

This study presents a detailed first-principles investigation of oxygen-deficient $CaMnO_{3-\delta}$, revealing how structural, electronic, and energetic properties evolve with increasing oxygen vacancy concentration. The introduction of vacancies leads to anisotropic lattice distortions, octahedral tilting, and nonlinear changes in bond lengths and angles. These structural changes are accompanied by a redistribution of electronic charge, particularly a reduction in the Mn oxidation state, as confirmed by Bader charge analysis.

The electronic band structure undergoes significant modifications, with the bandgap narrowing, and eventually closing, at intermediate δ levels, followed by the emergence of defect states and partial reopening at higher concentrations. This tunable electronic behavior highlights the potential of $CaMnO_{3-\delta}$ for applications requiring variable conductivity.

The calculated oxygen vacancy formation energies increase nonlinearly with δ, indicating that while low vacancy concentrations are energetically accessible, higher concentrations may require nonequilibrium synthesis conditions or lead to phase transitions. Notably, a relative stabilization around δ = 0.375 suggests a possible structural transition point, consistent with experimental observations of the phase change in $CaMnO_3$.

Overall, these results underscore the significant impact of oxygen vacancies on the structure of $CaMnO_{3-\delta}$ and the importance of resolving oxygen vacancies with high precision, as subtle but significant changes in properties may appear only at narrowly defined oxygen vacancy concentrations. The results also offer valuable new insights into the design of metal oxides with tailored electronic properties while also highlighting the need for further studies.

AUTHOR INFORMATION

Corresponding Author

Jonatan Gastaldi − *Department of Space, Earth, and Environment, Division of Energy technology, Chalmers University of Technology, Gothenburg SE-41296, Sweden*; orcid.org/0009-0006-4948-2209; Email: gastaldi@chalmers.se

Authors

Joakim Brorsson − *Department Physics, Division of Chemical Physics, Chalmers University of Technology, Gothenburg SE-41296, Sweden*

Anders Hellman − *Department Physics, Division of Chemical Physics and Competence Centre for Catalysis, Chalmers University of Technology, Gothenburg SE-41296, Sweden*; orcid.org/0000-0002-1821-159X

Tobias Mattisson − *Department of Space, Earth, and Environment, Division of Energy technology, Chalmers University of Technology, Gothenburg SE-41296, Sweden*; orcid.org/0000-0003-3942-7434

Complete contact information is available at: https://pubs.acs.org/10.1021/acs.jpcc.5c06816

Author Contributions

J.G.: Conceptualization; visualization; writing—original draft. J.B.: Conceptualization; writing—Review and editing. A.H.: Supervision; writing—review and editing. T.M.: Supervision; writing—review and Editing.

Notes

The authors declare no competing financial interest.

ACKNOWLEDGMENTS

This work was funded by the Swedish Research Council through grant agreement no. 2020-03487 and the computations were enabled by resources provided by the National Academic Infrastructure for Supercomputing in Sweden (NAISS) at NSC and PDC through projects 2023/3-29, 2023/5-147, 2023/5-521, 2024/5-260.

REFERENCES

(1) Li, T. T.; Yang, Y. B.; Li, G. R.; Chen, P.; Gao, X. P. Two-terminal perovskite-based tandem solar cells for energy conversion and storage. *Small* **2021**, *17*, No. 2006145.

(2) Mushtaq, S.; Tahir, S.; Ashfaq, A.; Almufarij, R. S.; Alqurashi, R. S.; Shokralla, E. A.; H-E, M. M. S.; Baig, A.; Alrefaee, S. H.; Almotairy, A. R. Z. Optimizing lead-free chalcogenide perovskite solar cells: a path to high efficiency and stability for renewable energy conversion. *Energy Fuels* **2024**, *38*, 3275−3287.

(3) Romano, V.; Agresti, A.; Verduci, R.; D'Angelo, G. Advances in perovskites for photovoltaic applications in space. *ACS Energy Lett.* **2022**, *7*, 2490−2514.

(4) Shikoh, A. S.; Polyakov, A. A quantitative analysis of the research trends in perovskite solar cells in 2009−2019. *Phys. Status Solidi A* **2020**, *217*, No. 2000441.
(5) Zhang, L.; Mei, L.; Wang, K.; Lv, Y.; Zhang, S.; Lian, Y.; Liu, X.; Ma, Z.; Xiao, G.; Liu, Q.; et al. Advances in the application of perovskite materials. *Nano-Micro Lett.* **2023**, *15*, No. 177.
(6) Liu, L.; Li, Z.; Wang, Y.; Li, Z.; Larring, Y.; Cai, N. Industry-scale production of a perovskite oxide as oxygen carrier material in chemical looping. *Chem. Eng. J.* **2022**, *431*, No. 134006.
(7) Dawa, T.; Sajjadi, B. Exploring the potential of perovskite structures for chemical looping technology: A state-of-the-art review. *Fuel Process. Technol.* **2024**, *253*, No. 108022.
(8) Poeppelmeier, K.; Leonowicz, M.; Scanlon, J.; Longo, J.; Yelon, W. Structure determination of CaMnO3 and CaMnO2. 5 by X-ray and neutron methods. *J. Solid State Chem.* **1982**, *45*, 71−79.
(9) Rørmark, L.; Mørch, A. B.; Wiik, K.; Stølen, S.; Grande, T. Enthalpies of oxidation of CaMnO3-*δ*, Ca2MnO4-*δ* and SrMnO3-*δ* deduced redox properties. *Chem. Mater.* **2001**, *13*, 4005−4013.
(10) Wang, Y.; Sui, Y.; Cheng, J.; Wang, X.; Lu, Z.; Su, W. High temperature metal− insulator transition induced by rare-earth doping in perovskite CaMnO3. *J. Phys. Chem. C* **2009**, *113*, 12509−12516.
(11) Zhang, F.; Lu, Q.; Zhang, X.; Zhang, J. First principle investigation of electronic structure of CaMnO3 thermoelectric compound oxide. *J. Alloys Compd.* **2011**, *509*, 542−545.
(12) Aschauer, U.; Pfenninger, R.; Selbach, S. M.; Grande, T.; Spaldin, N. A. Strain-controlled oxygen vacancy formation and ordering in CaMnO 3. *Phys. Rev. B* **2013**, *88*, No. 054111.
(13) Molinari, M.; Tompsett, D. A.; Parker, S. C.; Azough, F.; Freer, R. Structural, electronic and thermoelectric behaviour of CaMnO 3 and CaMnO (3−*δ*). *J. Mater. Chem. A* **2014**, *2*, 14109−14117.
(14) Marthinsen, A.; Grande, T.; Selbach, S. M. Microscopic link between electron localization and chemical expansion in AMnO3 and ATiO3 perovskites (A= Ca, Sr, Ba). *J. Phys. Chem. C* **2020**, *124*, 12922−12932.
(15) Mastronardo, E.; Qian, X.; Coronado, J. M.; Haile, S. M. Impact of La doping on the thermochemical heat storage properties of CaMnO3-*δ*. *J. Energy Storage* **2021**, *40*, No. 102793.
(16) Grimm, B.; Bredow, T. Oxygen Defect Formation Thermodynamics of CaMnO3: A Closer Look. *Phys. Status Solidi (b)* **2023**, *260*, No. 2200427.
(17) Merkulov, O.; Shamsutov, I.; Ryzhkov, M.; Politov, B.; Baklanova, I.; Chulkov, E.; Zhukov, V. Impact of oxygen vacancies on thermal and electronic transport of donor-doped CaMnO3-*δ*. *J. Solid State Chem.* **2023**, *326*, No. 124231.
(18) Grimm, B.; Bredow, T. Theoretical Study on Proton Migration on the CaMnO3 Surface. *J. Phys. Chem. C* **2024**, *128*, 12792−12798.
(19) Grimm, B.; Bredow, T. Revisiting CaMnO3 as a Proton Conductor—A Theoretical Perspective. *J. Phys. Chem. C* **2024**, *128*, 5429−5435.
(20) Abdel-Khalek, E. K.; Mohamed, E.; Ismail, Y. A. Study the role of oxygen vacancies and Mn oxidation states in nonstoichiometric CaMnO3-*δ* perovskite nanoparticles. *J. Sol−Gel Sci. Technol.* **2025**, *113*, 461−472.
(21) Gastaldi, J.; Brorsson, J.; Stanicic, I.; Hellman, A.; Mattisson, T. First-Principles Estimation of Thermodynamic Properties and Phase Stability of CaMnO3− *δ* for Chemical-Looping Combustion. *Energy Fuels* **2025**, *39*, 9113−9120.
(22) Hallberg, P.; Källén, M.; Jing, D.; Snijkers, F.; van Noyen, J.; Rydén, M.; Lyngfelt, A. Experimental Investigation of CaMnO3− *δ* Based Oxygen Carriers Used in Continuous Chemical-Looping Combustion. *Int. J. Chem. Eng.* **2014**, *2014*, No. 412517.
(23) Hallberg, P.; Rydén, M.; Mattisson, T.; Lyngfelt, A. CaMnO3-*δ* made from low cost material examined as oxygen carrier in Chemical-Looping Combustion. *Energy Procedia* **2014**, *63*, 80−86.
(24) Han, X.; Hu, Y.; Yang, J.; Cheng, F.; Chen, J. Porous perovskite CaMnO 3 as an electrocatalyst for rechargeable Li−O 2 batteries. *Chem. Commun.* **2014**, *50*, 1497−1499.
(25) Galinsky, N.; Mishra, A.; Zhang, J.; Li, F. Ca1− xAxMnO3 (A= Sr and Ba) perovskite based oxygen carriers for chemical looping with oxygen uncoupling (CLOU). *Appl.energy* **2015**, *157*, 358−367.
(26) Baranovskiy, A.; Amouyal, Y. Structural stability of calcium-manganate based CaO (CaMnO3) m (m= 1, 2, 3,∞) compounds for thermoelectric applications. *J. Alloys Compd.* **2016**, *687*, 562−569.
(27) Imponenti, L.; Albrecht, K. J.; Braun, R. J.; Jackson, G. S. Measuring thermochemical energy storage capacity with redox cycles of doped-CaMnO3. *ECS Trans.* **2016**, *72*, No. 11.
(28) Moldenhauer, P.; Hallberg, P.; Biermann, M.; Snijkers, F.; Albertsen, K.; Mattisson, T.; Lyngfelt, A. Oxygen-Carrier Development of Calcium Manganite−Based Materials with Perovskite Structure for Chemical-Looping Combustion of Methane. *Energy Technol.* **2020**, *8*, No. 2000069.
(29) Rosa, J.; Torres, S.; Thomazini, D.; Gelfuso, M. Microwave sintering of CaMnO3 thermoelectric perovskites synthesized by modified Pechini method. *Mater. Sci. Eng.: B* **2024**, *299*, No. 116956.
(30) Voitic, G.; Hacker, V. Recent advancements in chemical looping water splitting for the production of hydrogen. *RSC Adv.* **2016**, *6*, 98267−98296.
(31) Dieringer, P.; Marx, F.; Alobaid, F.; Ströhle, J.; Epple, B. Process control strategies in chemical looping gasification—a novel process for the production of biofuels allowing for net negative CO2 emissions. *Appl. Sci.* **2020**, *10*, No. 4271.
(32) Padak, B. Overview of Chemical Looping Technologies for Process Intensification: A Perspective. *Chem. Eng. Process.* **2024**, *205*, No. 110005.
(33) Rydén, M.; Leion, H.; Mattisson, T.; Lyngfelt, A. Combined oxides as oxygen-carrier material for chemical-looping with oxygen uncoupling. *Appl. Energy* **2014**, *113*, 1924−1932.
(34) Bakken, E.; Norby, T.; Stølen, S. Nonstoichiometry and reductive decomposition of CaMnO3− *δ*. *Solid State Ionics* **2005**, *176*, 217−223.
(35) Mattisson, T. Materials for chemical-looping with oxygen uncoupling. *Int. Scholarly Res. Not.* **2013**, *2013*, No. 526375.
(36) Jain, A.; Ong, S. P.; Hautier, G.; Chen, W.; Richards, W. D.; Dacek, S.; Cholia, S.; Gunter, D.; Skinner, D.; Ceder, G.; Persson, K. A. Commentary: The Materials Project: A materials genome approach to accelerating materials innovation. *APL Mater.* **2013**, *1*, No. 011002.
(37) Ångqvist, M.; Muñoz, W. A.; Rahm, J. M.; Fransson, E.; Durniak, C.; Rozyczko, P.; Rod, T. H.; Erhart, P. ICET−a Python library for constructing and sampling alloy cluster expansions. *Adv. Theory Simul.* **2019**, *2*, No. 1900015.
(38) Larsen, P. M.; Jacobsen, K. W.; Schiøtz, J. Rich ground-state chemical ordering in nanoparticles: Exact solution of a model for Ag-Au clusters. *Phys. Rev. Lett.* **2018**, *120*, No. 256101.
(39) Brorsson, J.; Palmqvist, A. E.; Erhart, P. First-principles study of order−disorder transitions in pseudobinary clathrates. *J. Phys. Chem. C* **2021**, *125*, 22817−22826.
(40) Kresse, G.; Furthmüller, J. Efficient iterative schemes for ab initio total-energy calculations using a plane-wave basis set. *Phys. Rev. B* **1996**, *54*, No. 11169.
(41) Ong, S. P.; Richards, W. D.; Jain, A.; Hautier, G.; Kocher, M.; Cholia, S.; Gunter, D.; Chevrier, V. L.; Persson, K. A.; Ceder, G. Python Materials Genomics (pymatgen): A robust, open-source python library for materials analysis. *Comput. Mater. Sci.* **2013**, *68*, 314−319.
(42) Perdew, J. P.; Burke, K.; Ernzerhof, M. Generalized gradient approximation made simple. *Phys. Rev. Lett.* **1996**, *77*, No. 3865.
(43) Togo, A. First-principles phonon calculations with phonopy and phono3py. *J. Phys. Soc. Jpn.* **2023**, *92*, No. 012001.
(44) Reuter, K.; Scheffler, M. Composition, structure, and stability of RuO 2 (110) as a function of oxygen pressure. *Phys. Rev. B* **2001**, *65*, No. 035406.
(45) Tables, J. T. *NSRDS-NBS37*; National Bureau of Standards Publication, 1971.
(46) Becke, A. D.; Johnson, E. R. A simple effective potential for exchange. *J. Chem. Phys.* **2006**, *124*, No. 221101, DOI: 10.1063/1.2213970.

(47) Tran, F.; Blaha, P.; Schwarz, K. Band gap calculations with Becke−Johnson exchange potential. *J. Phys.: Condens. Matter* **2007**, *19*, No. 196208.
(48) M Ganose, A.; Jackson, A. J.; Scanlon, D. O. sumo: Command-line tools for plotting and analysis of periodic* ab initio* calculations. *J. Open Source Software* **2018**, *3*, No. 717.
(49) Jung, J. H.; Kim, K.; Eom, D.; Noh, T.; Choi, E.; Yu, J.; Kwon, Y.; Chung, Y. Determination of electronic band structures of CaMnO 3 and LaMnO 3 using optical-conductivity analyses. *Phys. Rev. B* **1997**, *55*, No. 15489.
(50) Panigrahi, R.; Mallik, B. S. Ionic conduction and cathodic properties of CaMO3 (M= Fe and Mn) electrode materials via molecular dynamics and first-principles simulations. *J. Phys. Chem. Solids* **2025**, *196*, No. 112384.
(51) Søndenå, R.; Stølen, S.; Ravindran, P.; Grande, T.; Allan, N. L.; et al. Corner-versus face-sharing octahedra in A Mn O 3 perovskites (A= Ca, Sr, and Ba). *Phys. Rev. B* **2007**, *75*, No. 184105.
(52) Leion, H.; Larring, Y.; Bakken, E.; Bredesen, R.; Mattisson, T.; Lyngfelt, A. Use of CaMn0. 875Ti0. 125O3 as oxygen carrier in chemical-looping with oxygen uncoupling. *Energy Fuels* **2009**, *23*, 5276−5283.
(53) Li, X.; Faust, R.; Purnomo, V.; Mei, D.; Linderholm, C.; Lyngfelt, A.; Mattisson, T. Performance of a perovskite-structured calcium Manganite oxygen carrier produced from natural ores in a batch reactor and in operation of a chemical-looping combustion reactor system. *Chem. Eng. J.* **2024**, *497*, No. 154516.
(54) Momma, K.; Izumi, F. VESTA 3 for three-dimensional visualization of crystal, volumetric and morphology data. *J. Appl. Crystallogr.* **2011**, *44*, 1272−1276.
(55) Guiblin, N.; Grebille, D.; Leligny, H.; Martin, C. Ca3Mn2O7. *Cryst. Struct. Commun.* **2002**, *58*, i3−i5.
(56) Leonowicz, M.; Poeppelmeier, K. R.; Longo, J. Structure determination of Ca2MnO4 and Ca2MnO3. 5 by X-ray and neutron methods. *J. Solid State Chem.* **1985**, *59*, 71−80.
(57) Chiang, C. C.; Poeppelmeier, K. R. Structural investigation of oxygen-deficient perovskite CaMnO2. 75. *Mater. Lett.* **1991**, *12*, 102−108.
(58) Takahashi, J.; Kamegashira, N. X-ray structural study of calcium manganese oxide by rietveld analysis at high temperatures [Ca2MnO4. 00]. *Mater. Res. Bull.* **1993**, *28*, 565−573.
(59) Chihaoui, N.; Dhahri, R.; Bejar, M.; Dharhi, E.; Costa, L.; Graça, M. Electrical and dielectric properties of the Ca2MnO4− δ system. *Solid State Commun.* **2011**, *151*, 1331−1335.
(60) Surace, Y.; Simões, M.; Eilertsen, J.; Karvonen, L.; Pokrant, S.; Weidenkaff, A. Functionalization of Ca2MnO4−δ by controlled calcium extraction: Activation for electrochemical Li intercalation. *Solid State Ionics* **2014**, *266*, 36−43.

https://doi.org/10.1021/acs.jpcc.5c06816
J. Phys. Chem. C 2026, 130, 1726−1735